Proceedings of the IMAC-XXVIII
February 1–4, 2010, Jacksonville, Florida USA

Underwater Explosion Phenomena and Shock Physics

Frederick A. Costanzo
Naval Surface Warfare Center Carderock Division, UERD
9500 MacArthur Boulevard
West Bethesda, MD 20817-5700
(301) 227-1650

NOMENCLATURE

C_0	Nominal Sound Speed
D	Depth of Charge
e	Exponential Function
E	Energy Flux Density
FT	Feet
G/CC	Grams per Cubic Centimeter
I	Impulse per Unit Area
IN	Inches
lbs, LB, #	Pounds
M/SEC	Meters per Second
msec	Milliseconds
P	Pressure
P_0	Peak Incident Pressure
P(t)	Pressure as a Function of Time
psi	Pounds per Square Inch
R	Range
sec	Seconds
t	Time
W	Explosive Charge Weight
Wi	Image Charge
ρ_0	Nominal Mass Density
θ	Shock Wave Decay Constant

ABSTRACT

This paper presents a brief introduction to the basic fundamentals of underwater explosions, including discussion of the features of explosive charge detonation, the formation and characterization of the associated shock wave, bulk cavitation effects, gas bubble formation and dynamics, surface effects and shock wave refraction characteristics. Illustrations of each of these fundamental aspects of underwater explosion (UNDEX) loadings are made with a set of videos from a variety of experimental testing events. In addition, analyses of associated measured loading and dynamic response data, as well as descriptions of supporting numerical simulations of these events are presented. At the conclusion of this paper, each of these UNDEX effects are tied together with a summary discussion and illustration.

INTRODUCTION

The field of underwater explosions and shock physics is both complex and fascinating. There are many aspects of the underwater explosion event that must be studied in order to properly understand the development and propagation of the dynamic shock loading through the fluid. The following sections of this paper provide an introduction to the basic features associated with the underwater detonation of an explosive charge [1], dividing the discussion into a series of primary features. These features include: the explosion or detonation phase, the formation of the shock wave and its effects, the secondary loading effect known as bulk cavitation, the effects of the expanding and contracting gas bubble, observed surface effects, and shock wave refraction effects. Each of these features will be described in some level of detail, and then all of these features will be summarized as they collectively form a composite illustration of underwater explosion phenomena.

Fig. 1 below illustrates a typical underwater explosion event against a full scale ship target. In these types of events, all of the features outlined above and described within this paper play an important role in defining the dynamic loadings that are imparted to the ship, as well as in the visual effects that are observed in the vicinity of the event. It is the objective of this paper to provide a detailed enough introduction of these phenomena that a deeper understanding of the basic physics involved will be attained.

Fig. 1 – Typical Underwater Explosion Test of a Full Scale Ship Target

EXPLOSION PHASE

The underwater detonation of an explosive charge can best be described as an exothermic chemical reaction that is self-sustaining after initiation. Forming throughout the detonation process are gaseous reactive components that are at an extremely high temperature (approximately 3000 degrees Celsius) and pressure (approximately 50000 atmospheres). The entire detonation process represents a rapidly propagating reaction, with propagation speeds in the neighborhood of 25000 feet per second.

Shown below in Fig. 2 are examples of typical explosives. Presented for each explosive listed are its explosive name, its chemical composition, as well as its specific gravity and detonation velocity. The most common and well-known explosive type is TNT, which is most often used as the standard when comparing energy and impulse yields of the other types of explosives. RDX is another common type of explosive. Most of the other explosives listed are essentially compositions of TNT, RDX and other additives in order to produce the desired effects. The exception to this is PBXN-103, which is composed of a variety of different elements. Explosives such as COMP B, H-6, HBX-1 and HBX-3 all have aluminum added in order to enhance the late-time burn and thus generate greater bubble energy. HBX-1, due to its stability and availability, is the most common explosive used by the Navy for shock qualification purposes and full ship shock trials. As can be seen from the chart in Fig. 2, there is a range of densities and detonation velocities associated with this group of explosives.

EXPLOSIVE	*FORMULA*	*DENSITY (G/CC)*	*DET. VELOCITY (M/SEC)*
TNT	$C_7H_5N_3O_6$	1.60	6940
RDX	$C_3H_6N_6O_6$	1.57	8940
COMP B	RDX/TNT/WAX 59.4/39.6/1.0	1.68	7900
H-6	RDX/TNT/AL/WAX 45.1/29.2/21.0/4.7	1.74	7440
PBXN-103	AP/AL/PNC/MTN/RESOURCINOL/TEGDN 38.73/27.19/6.92/24.36/0.36/2.44	1.89	6130
HBX-1	RDX/TNT/AL/WAX	1.72	7310
HBX-3	PBX/TNT/AL/WAX 31/29/35/5	1.82	7310

Fig. 2 – Examples of Common Explosives

FORMATION OF THE SHOCK WAVE

Upon detonation of the explosive charge, a very steep-fronted shock wave develops at the source and propagates rapidly in the surrounding fluid. A schematic diagram illustrating this shock wave propagation is shown in Fig. 3. In this diagram, one can see the shock wave propagating spherically away from the source of detonation, while at the center of detonation a gas bubble is forming at a much slower rate. To put things in proper perspective, the shock wave propagation phase is on the order of milliseconds, while the bubble expansion and contraction phase is on the order of seconds. Thus, there is about a three order of magnitude time scale difference for these two phenomena. Such a large difference as this in the time scales does pose challenges for some computational methods that intend to include both phases.

The shock wave propagation can be likened to the stress wave that propagates axially along an elastic rod that has been hit on one end with a hammer. Once the shock wave has formed and has propagated to distance beyond about 2-3 charge radii, the propagation speed remains constant and assumes linear acoustic behavior. Inside of 2-3 charge radii, however, the propagation is highly nonlinear. Most UNDEX applications involve intermediate or far field scenarios, and thus for these the acoustic propagation assumption is valid. For extremely close-in or near contact scenarios, the nonlinear propagation characteristics must be considered.

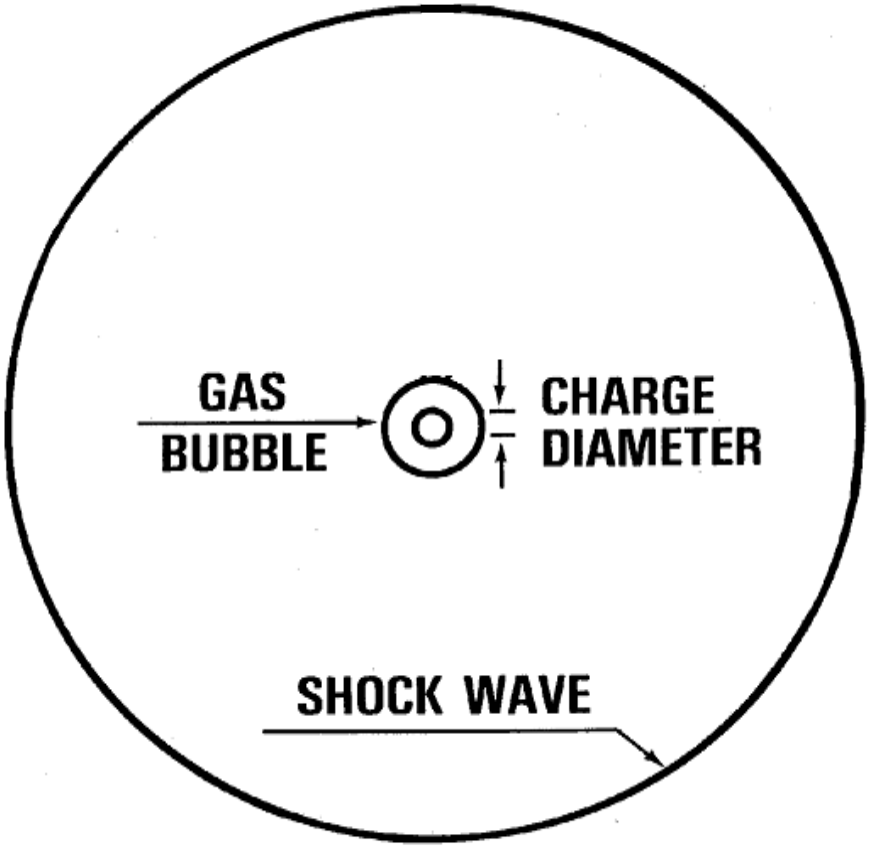

Fig. 3 – Shock Wave from an Underwater Explosion

In Fig. 4, the far field shock wave pressure for a conventional weapon is illustrated. As can be seen from the curve and expression for pressure as a function of time, the shock wave pressure varies as an exponential function. As a result, the pressure function starts out at a peak value of P_0 at time zero, and decays to 1/e or about 37% of its original value in θ milliseconds in time. Here θ is referred to as the decay constant. For the example provided in Fig. 4, which is for the case of a 250# HBX-1 explosive charge detonated at a distance of 50 ft from the gage point, the resulting pressure function has a peak value of about 2500 psi and decays exponentially down to a value of about 850 psi in 0.62 milliseconds. This exponential behavior of the free-field shock wave is extremely convenient and lends itself to straightforward computations when evaluating shock wave impulse and energy, as will be shown later. This exponential variation of the incident shock wave pressure is accurate for at least about one decay constant. After that point, the incident shock wave pressure actually begins to decay at a slower rate in the tail of the shock wave.

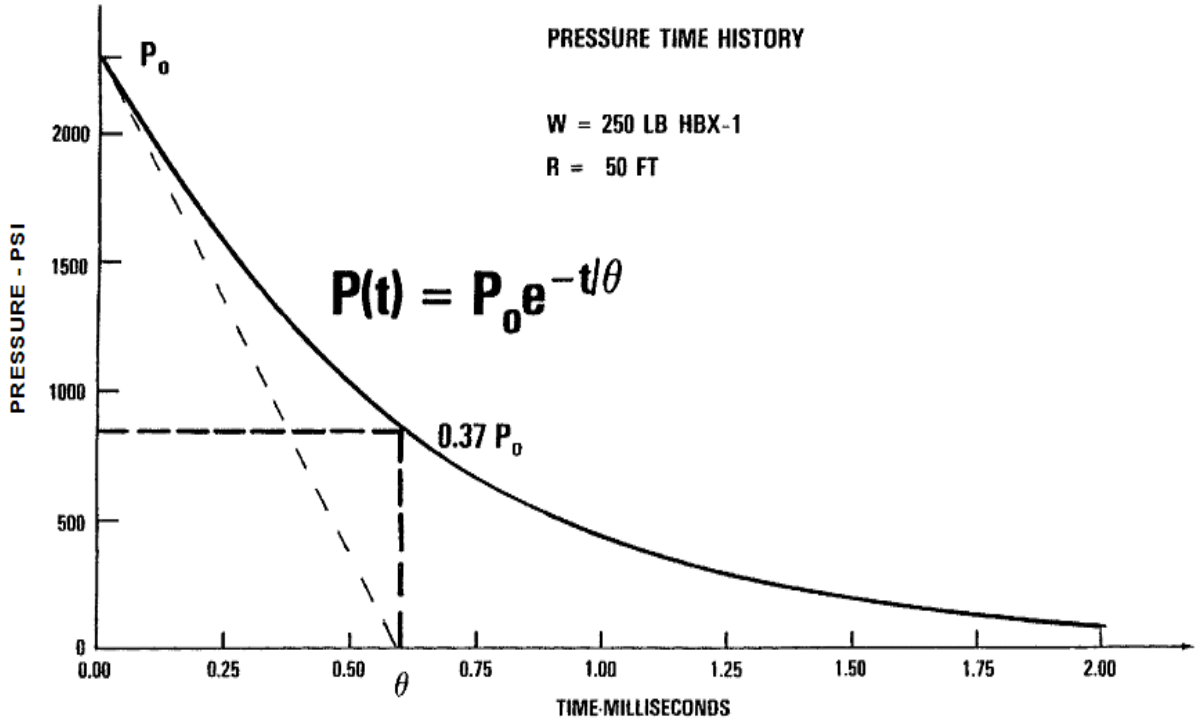

Fig. 4 – Shock Wave Pressure History for a Conventional Weapon

Next, the variation of shock wave pressure with range will be briefly discussed. Shown in Fig. 5 is a plot of the shock wave peak pressure vs. shock severity, expressed in the non-dimensional form of $W^{1/3}/R$, where W is the explosive charge weight and R is the standoff from the charge to the point of interest. From this curve, it can be observed that for a large range of standoff values, the variation of peak shock wave pressure with shock severity is linear. However, as one moves closer to the explosive charge source location, the peak pressure variation becomes nonlinear. This point was made earlier when describing the linear nature of the shock wave propagation for ranges greater than about 2-3 charge radii. Inside of this range, the acoustic approximation for shock wave propagation no longer is valid and nonlinear behavior begins to take place.

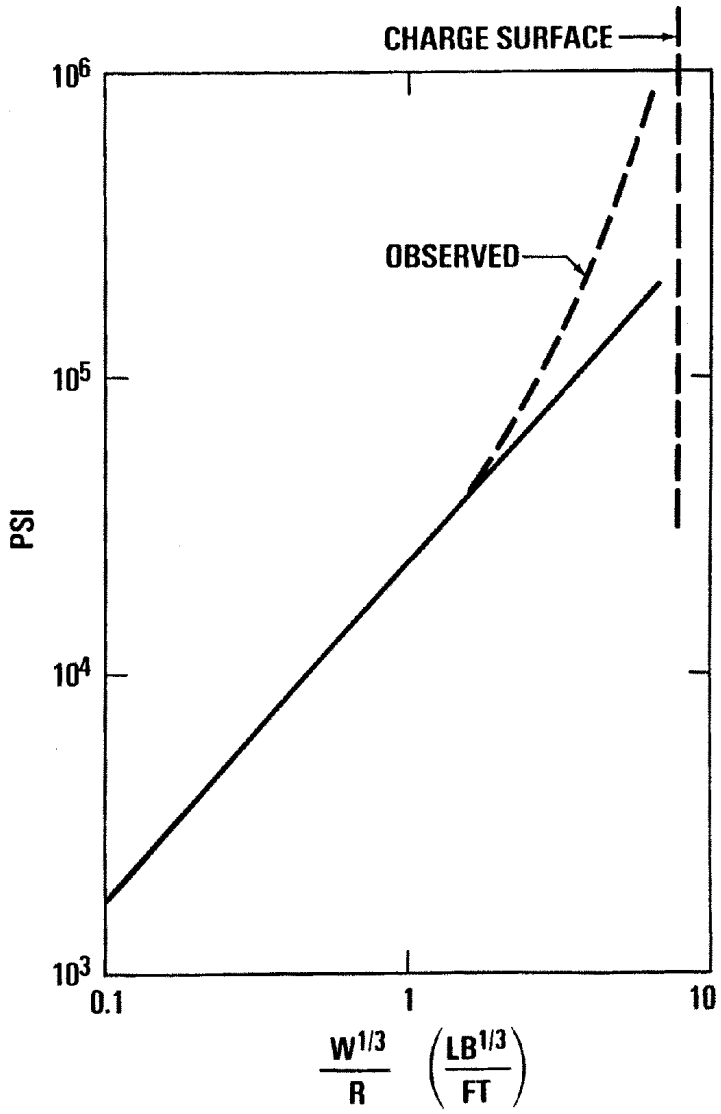

Fig. 5 - Variation of Shock Wave Pressure with $W^{1/3}/R$

The description of the shock wave pressure variation with time is summarized below in Fig. 6. Here for TNT, the relationship of peak shock wave pressure, P_0, and shock wave severity, $W^{1/3}/R$, is given as a power function. A similar power relationship is provided for the shock wave decay constant, θ. These relationships, referred to as shock wave similitude equations, were developed through a series of free-field experiments conducted by the Naval Ordnance Laboratory (NOL) in the 1950s and 1960s. In these experiments, a variety of explosive charge sizes were detonated in the vicinity of arrays of pressure transducers positioned at various ranges from the source. These resulting pressure measurements were then analyzed and regression analyses were conducted to determine the best curve fits relating peak shock wave pressure and decay constant to shock severity. The basic form of these power relations can be seen from Fig. 6 to be a coefficient multiplied by the non-dimensional term $W^{1/3}/R$ raised to a power. For the decay constant, θ, the power curve fit contains an additional $W^{1/3}$ term.

$$P(t) = P_0 e^{-t/\theta} \qquad 0 \le t \le \theta$$

For TNT:

$$P_0(\text{psi}) = 2.16 \bullet 10^4 \left(\frac{(W[\text{lbs}])^{1/3}}{R[\text{ft}]} \right)^{1.13}$$

$$\theta(\text{msec}) = 0.06\,(W[\text{lbs}])^{1/3} \left(\frac{(W[\text{lbs}])^{1/3}}{R[\text{ft}]} \right)^{-0.18}$$

Fig. 6 – Shock Wave Pressure Functional Form

When using these power relations, one must be aware of the limits of applicability of these curve fits. Each set of published similitude equations has associated with it the ranges of charge sizes and standoffs that were used in the experiments to obtain the pressure data. For values of explosive charge weight and standoff outside of these ranges the power relations may no longer be valid. Thus, it is extremely important for the user of these power relationships to fully understand the appropriate ranges of applicability.

Shown in Fig. 7 are the expressions for shock wave energy and impulse. For the shock wave energy expression, the energy per unit area, also know as the energy flux density, is expressed as $1/(\rho_0 C_0)$ times the integral of the square of the pressure with time. For the shock wave impulse, the impulse per unit area is expressed as simply the integral of the pressure function with time. Due to the exponential nature of the shock wave pressure function, these expressions for shock wave energy and impulse can easily be evaluated. Also, as was developed for the peak shock wave pressure and decay constant, power relationships for the both the shock wave energy and shock wave impulse were developed and are presented in Fig. 7. These empirical expressions were developed for specific values of the upper limit of integration of usually 3, 5 or 7 times the shock wave decay constant. As a result, the analyst is cautioned when using these to properly identify the appropriate version of the power fit for the particular problem at hand.

Finally, the concept of surface cutoff will now be described. From the diagram in Fig. 8, the direct path of the shock wave from the explosive source to the target is illustrated with the vector labeled R. This is the shortest path to the target and thus at the point of impingement, assuming time is dated from first arrival of the shock wave to the target and ignoring for the moment any shock wave reflections, the incident pressure would appear as shown in the lower of the two pressure-time curves given in the figure. However, due to the presence of the free surface and the fact that the shock wave propagates spherically away from the source, there is a second path that the incident shock wave takes that intersects the water surface. Due to the significant

SHOCKWAVE ENERGY

$$E = \frac{1}{\varrho_o C_o} \int_0^t P^2(t)\, dt$$

FOR TNT: $E = 2.44 \times 10^3\ W^{1/3}\ (W^{1/3}/R)^{2.04}$ $\left(\frac{IN - \#}{IN^2}\right)$

SHOCKWAVE IMPULSE

$$I = \int_0^t P(t)\, dt$$

FOR TNT: $I = 1.46\ W^{1/3}\ (W^{1/3}/R)^{0.89}$ $\left(\frac{\# SEC}{IN^2}\right)$

Fig. 7 – Shock Wave Energy and Impulse

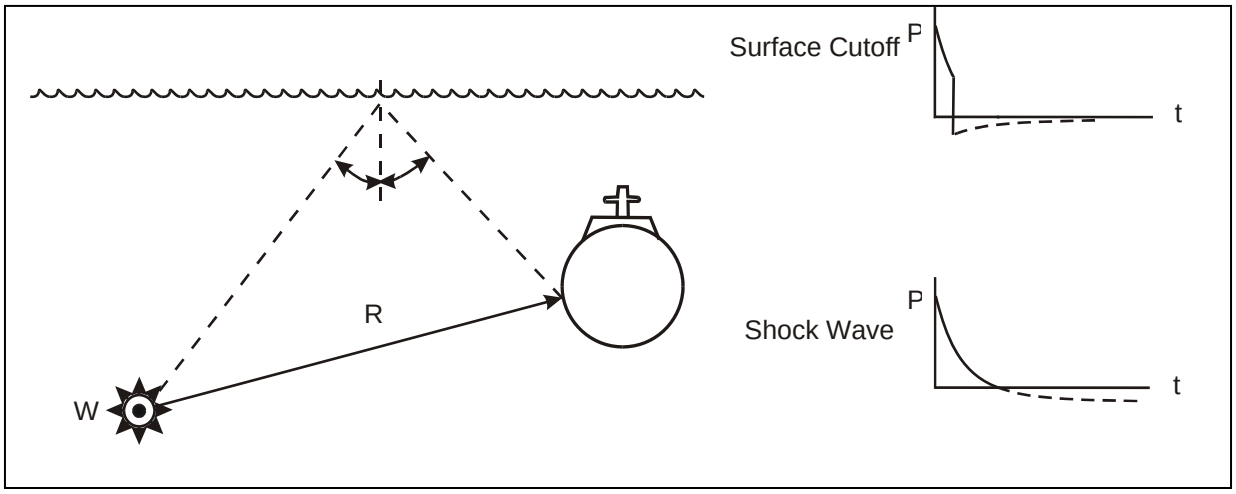

Fig. 8 – Illustration of Surface Cutoff

impedance mismatch between water and air, this reflection of the compressive shock wave with the free surface results in a tensile wave that is reflected back into the fluid. This reflected tensile wave subsequently propagates towards the target and arrives at the point of impingement at some finite time after the arrival of the incident shock wave. Upon arrival at the target, this tensile wave has the effect of suddenly reducing the amplitude of the loading pressure at the target, as shown in the upper pressure-time history shown in Fig. 8. This modification of the incident shock wave pressure is known as surface cutoff. The time delay associated with this surface cutoff can be computed by simply considering the respective paths of the direct and surface reflected shock waves, and is referred to as the surface cutoff time.

As can be seen from the surface cutoff illustration in Fig.8, reflections of the incident shock wave are extremely important and must all be considered as these reflections can significantly modify the dynamic loading that is imparted to the target. A more detailed illustration of shock wave reflections is presented in Fig. 9, where the effects of both a free surface and a reflecting ocean bottom can be observed. In this example, the pressure at a selected point in the fluid, P, which could represent a point on the target, is illustrated in the time history curve shown. Initially, the incident shock wave compressive pressure arrives at the point of interest and results in a sharp rise in pressure from zero gage pressure to the peak shock wave pressure. This pressure then begins to decay exponentially in time, as shown. At the same time this is occurring, another path that the incident shock wave travels is to the surface, and is then reflected back into the fluid as a tensile wave. This tensile wave arrives at the point of interest delayed in time from the direct shock wave and abruptly reduces the decayed incident shock wave pressure to some negative value. In addition to these two loading effects, there is a third path that the shock wave can travel and that is to the ocean bottom. Depending on the nature of the bottom material, the resulting reflected wave can vary between a strong compressive reflection to a weak tensile reflection. Normally, a reinforcing compressive wave is reflected and when this arrives at the point of interest, an enhancement of the current pressure amplitude will occur, as shown in the time history illustration in Fig, 8. This example illustrates the complex nature of identifying the dynamic loadings associated with an UNDEX event and the importance of considering all potential reflective sources present in the particular problem of interest.

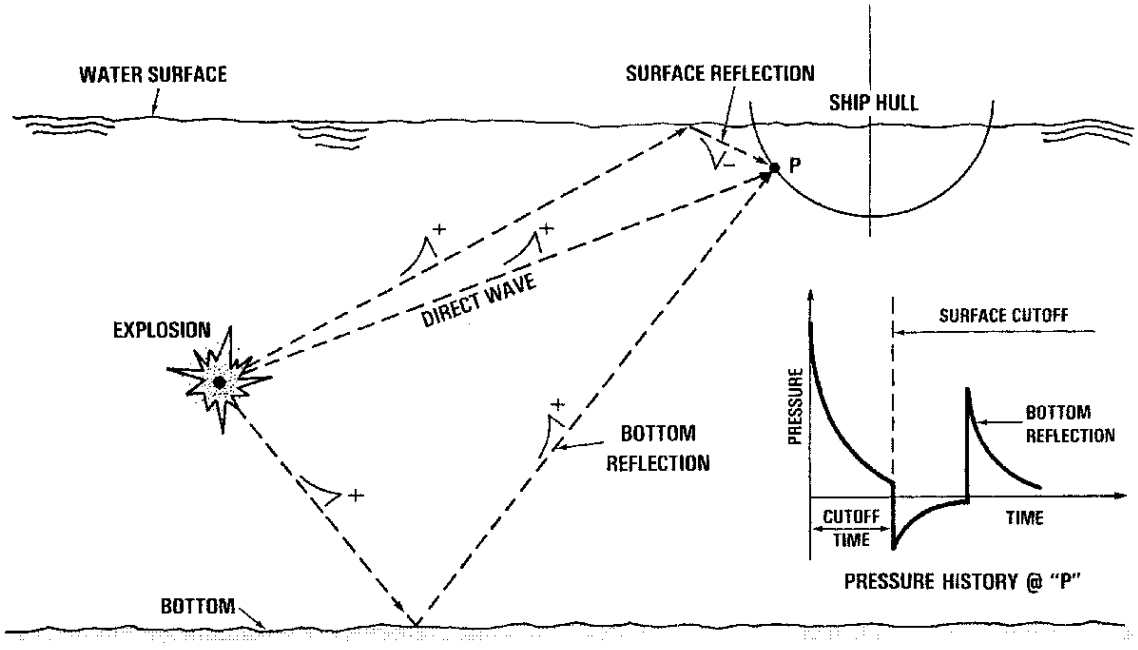

Fig. 9 – Shock Wave Reflections

BULK CAVITATION PHENOMENA

The next concept to be discussed is that of bulk cavitation [2]. Bulk cavitation occurs when a compressive shock wave travels to the surface and is reflected back into the fluid as a tensile wave. Since water cannot normally sustain a large amount of tension, it cavitates and thus is transformed from a continuous, homogeneous liquid into a non-homogeneous, vaporous region. This cavitated zone is thus incapable of further transmitting any shock disturbances in its current state. An illustration of the region of fluid that is ultimately affected by bulk cavitation is provided in Fig. 10. The region shown is not a snapshot in time, but an envelope showing the maximum extent of cavitated fluid over all time. The reason that bulk cavitation is of interest is that when the cavitated zone actually closes, due to the effects of gravity and atmospheric pressure from above and the flow from the expanding gas bubble from below, two significant fluid masses collide creating a water hammer effect and producing a secondary shock in the form of a compressive pulse. This compressive pulse, known as the bulk cavitation closure pulse, depending on the circumstances can represent a significant reloading of the target. A somewhat exaggerated depiction of the bulk cavitation closure pulse is shown with respect to the incident pressure and first bubble pulse. In most cases, the compressive bulk cavitation closure pulse will be detectable but is usually of reduced magnitude with respect to the primary shock and bubble pulses. However, certain explosive geometry scenarios can exist that bring about a more significant and possibly damaging bulk cavitation closure pressure pulse. As a result, all UNDEX test scenarios should explore the bulk cavitation dynamics in order to identify the possibility for a significant target reloading.

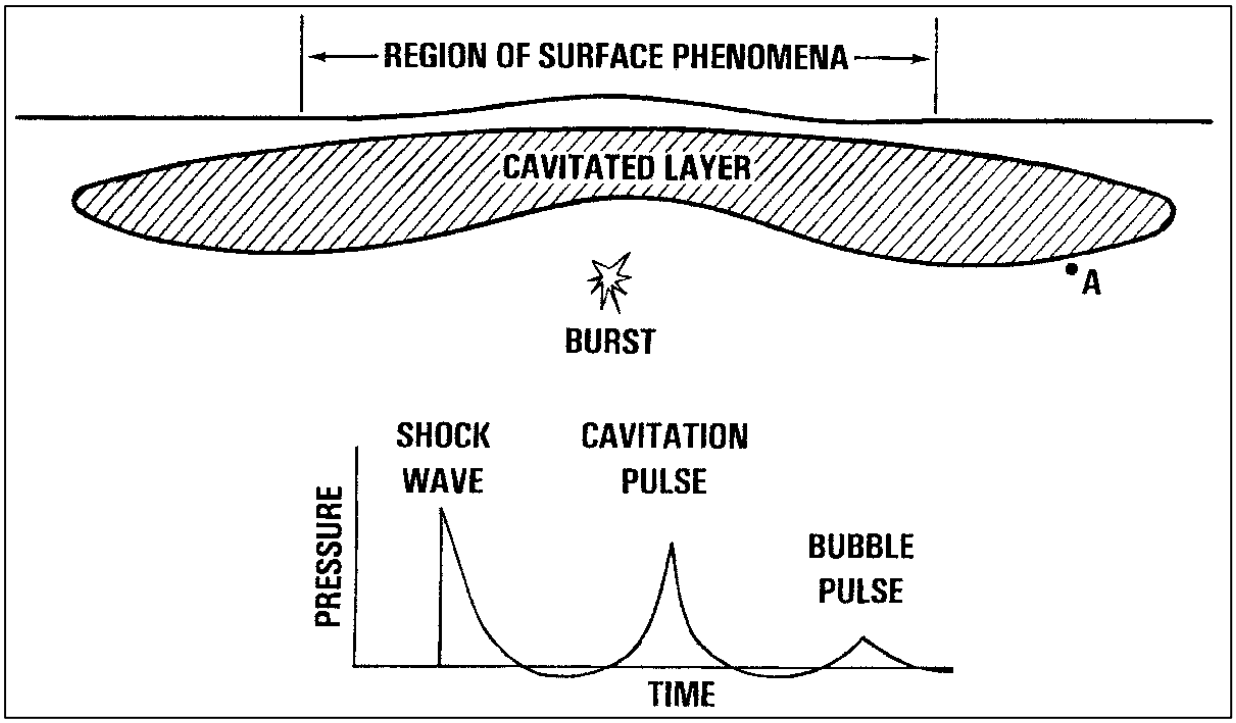

Fig. 10 – Effects of Bulk Cavitation of the Surface Layer

Illustrated in Fig. 11 are the propagation of the direct incident shock wave and its surface reflected counterpart. As the spherical compressive shock front moves through the fluid, it loads any structures that are within its path. Trailing behind this shock front is the spherical surface reflected tensile wave that sweeps through and tries to reduce the total pressure in the fluid to below the vapor pressure. As a result, a state of cavitation is produced in the fluid as this "relief" wave sweeps through. The maximum extent of the bulk cavitation region that occurs over time is depicted by the boundaries in Fig. 11 that separate the white cavitated region from the blue uncavitated fluid. As mentioned earlier, this is not a snapshot in time.

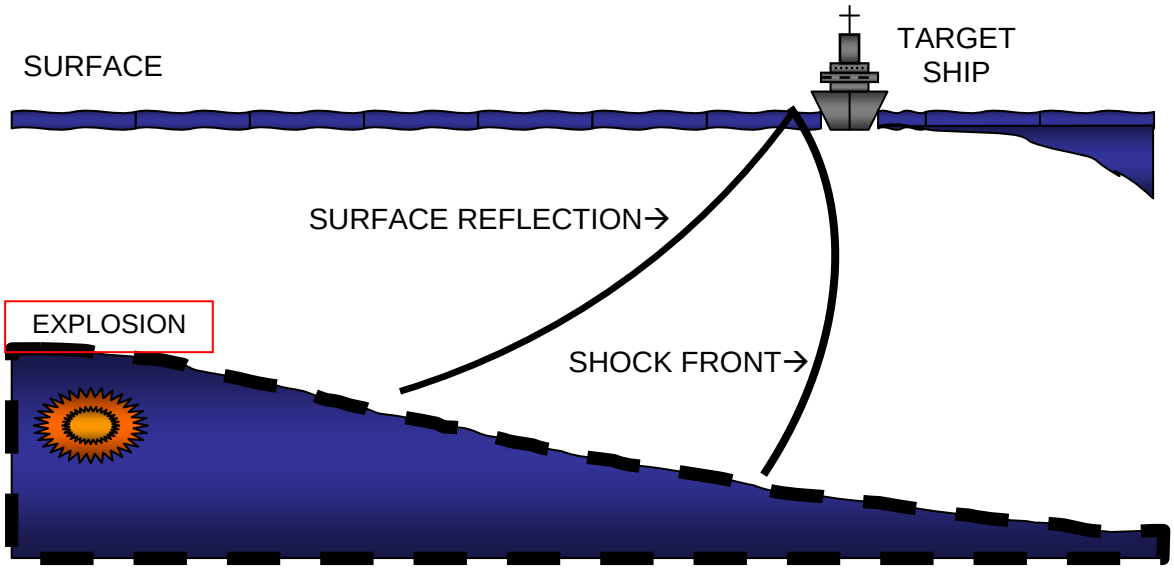

Fig. 11 – Illustration of the Formation of the Bulk Cavitation Region

The illustration in Fig. 12, however, with the arrows indicating the direction that the boundaries are moving, does represent a snaphot in time of the opening and closure of the bulk cavitation region. Here it is convenient to depict the surface reflection as emanating from an image charge located at a distance, D, above the water surface. As the shock front and trailing surface reflection front are passing through the region towards the right hand side of this sketch, the forces of atmospheric pressure and gravity, along with the flow from the expanding gas bubble, are forcing the two surfaces to collide. This point of collision, referred to as the point of first closure, normally occurs at a point that is about ¼ of the total extent of the cavitated region. This closure impact then propagates like a zipper going in the directions away from and towards the charge location. The result of these cavitation closure dynamics is to produce compressive shock impulses that reload the target. The process continues until the cavitation zone is completely closed. As the cavitation closure pulses propagate to the surface and are subsequently reflected back into the fluid as tensile waves, additional cavitations can occur until all of the available energy is dissipated.

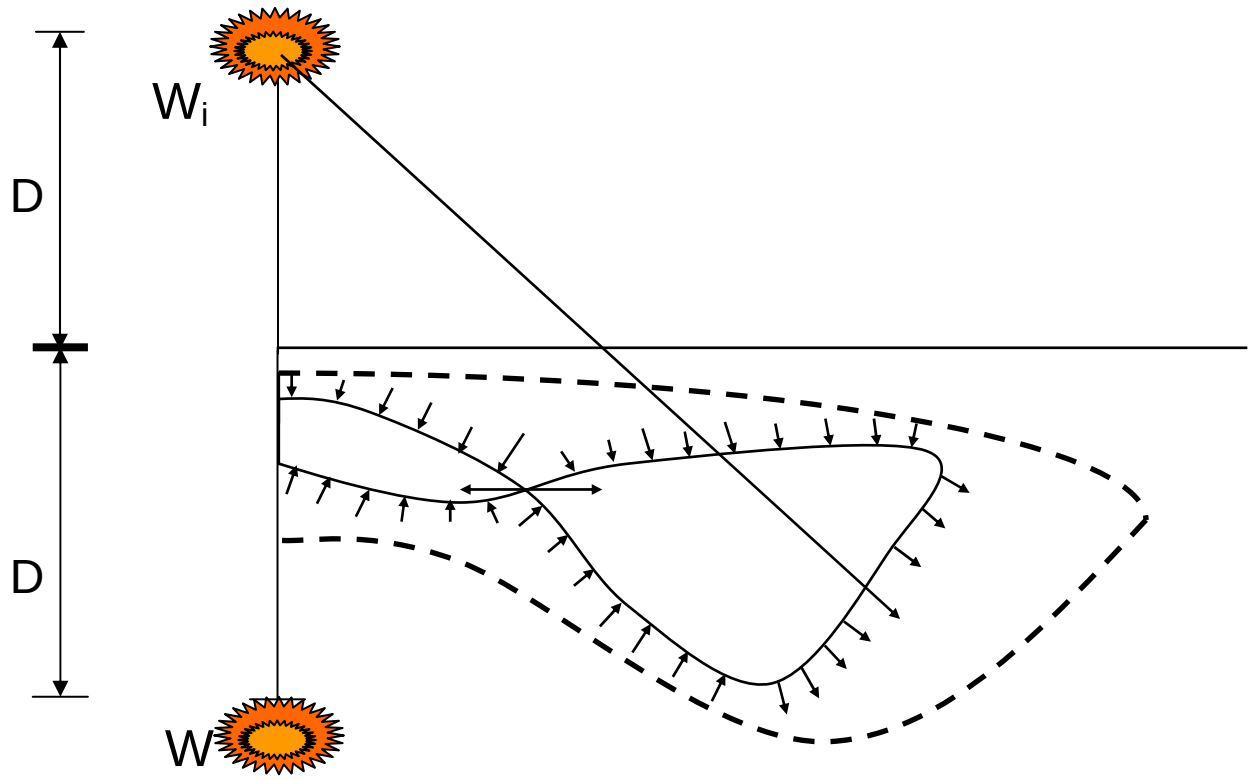

Fig. 12 – Closure of the Bulk Cavitation Region

Finally, a summary of the UNDEX shock environment associated with the incident shock wave, surface reflected wave, bottom reflected wave, and the opening and closure of the bulk cavitation region is illustrated by the collection of snapshots in time and associated pressure-time history shown in Fig. 13. The snapshots shown are animations from a free-field analysis of a shock scenario using a hydrocode. For this application, the explosive charge is placed approximately midway between the surface and a hard reflecting ocean bottom. Shortly after the explosive charge is detonated, the snapshot shown is the upper left was generated. This schematic shows the incident pressure wave emanating directly from the charge at the left. A black dot at the edge of the compressive shock front represents a pressure reference point. Also seen from this schematic is the compressive wave reflection off of the sea bottom and its propagation throughout the fluid and the bottom material. In the upper left hand portion of this same snapshot one can also see the formation of the bulk cavitation region (white area) as the surface reflected wave propagates through the fluid from upper left to lower right. By analyzing the pressure at the point of interest (black dot) associated with the snapshots at the top and bottom left of the figure, one can see in chronological order the arrival of incident shock wave pressure and its subsequent exponential decay, the arrival of the bottom reflected compressive wave that occurs an instant before the arrival of the surface reflected wave, and the effect of the surface reflected wave that reduces the pressure at this point down to the cavitation pressure.

During the next phase of response, a state of cavitation exists at the gage point as is manifested by the constant slightly negative pressure in the corresponding time history. This is associated with the snapshot shown in the upper right hand side of Fig. 13. This state of cavitation exists until the atmospheric pressure, gravity and gas bubble flow work to close this region.

Finally, as the cavitated region closes, as depicted in the snapshot in the lower right hand side of Fig. 13, the associated pressure-time history indicates the effects of the compressive closure pulse. Although the closure pulse in this example has a low amplitude when compared with the incident shock wave peak pressure, it does have a rather significant impulse associated with it. This is the kind of later time impulse that can significantly reload a structure and once again points to the importance of considering all of the aspect of the UNDEX event.

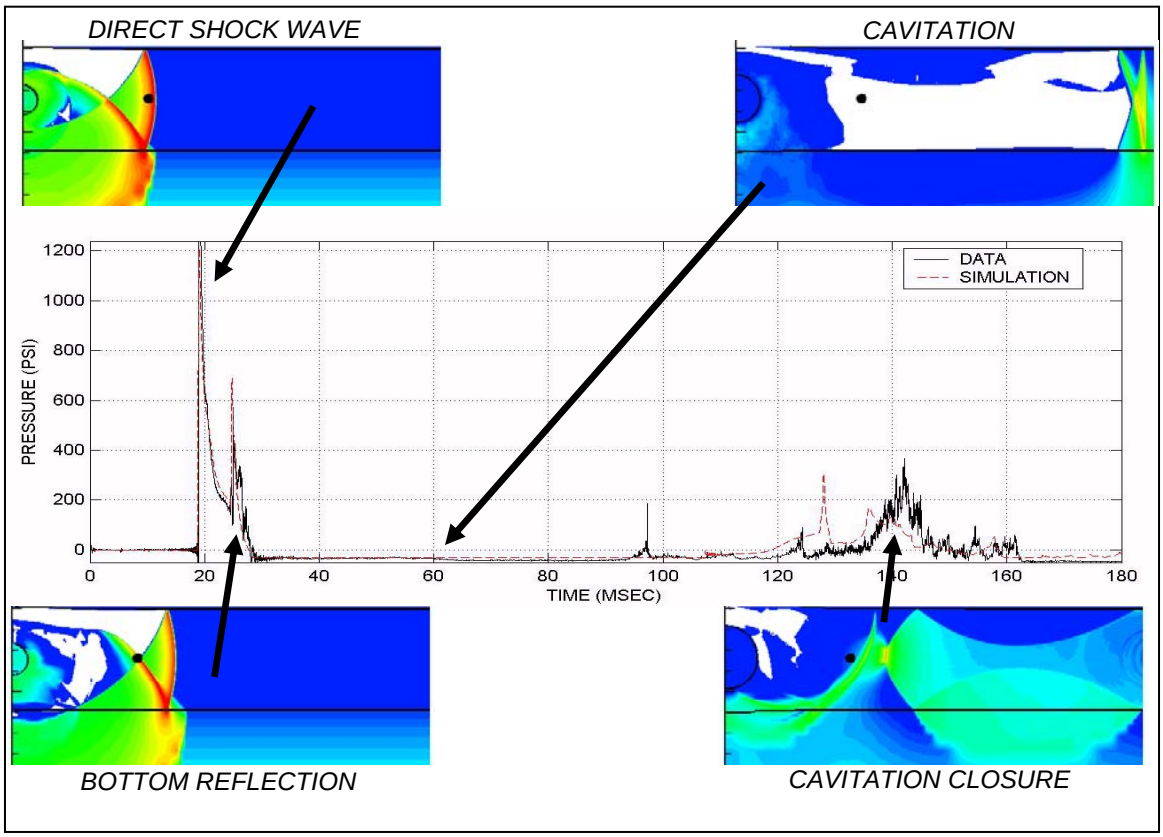

Fig. 13 – UNDEX Shock Environment

GAS BUBBLE DYNAMICS

In the earlier discussion describing the detonation of an explosive charge, two primary physical aspects of the UNDEX event were shown to develop. The first aspect of the UNDEX event, the formation and propagation of the shock wave, was described in detail, and was observed to last on the order of milliseconds. The second primary aspect of the UNDEX event, the expansion, contraction and migration of the gas bubble [3], will now be described. This aspect of response occurs within a time frame that is on the order of seconds. To introduce this aspect of response, the diagram shown in Fig. 14 will now be explained in detail. This diagram illustrates different phases of bubble growth, contraction and migration, and associates them with corresponding phases of a pressure-time history.

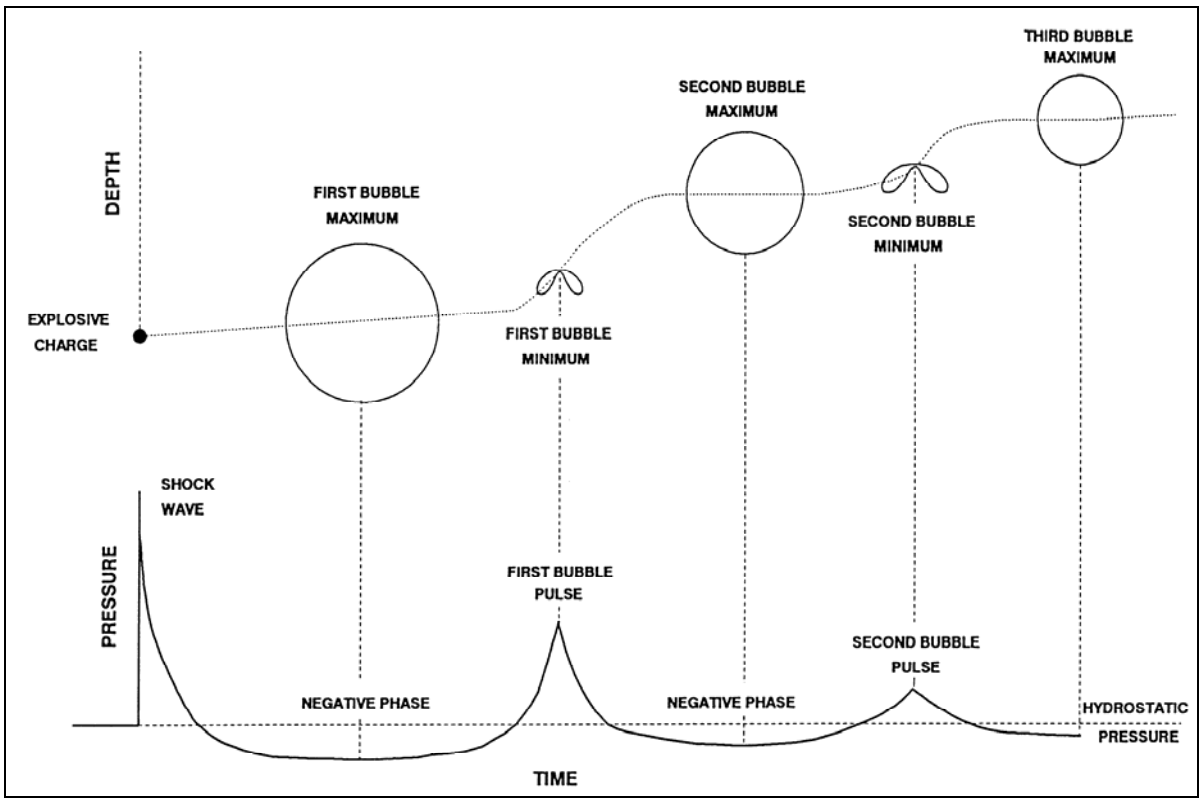

Fig. 14 – Explosion Bubble Phases and Pressure-Time History

The initial part of the time history show in Fig. 14 shows the incident shock wave pressure and its exponential decay phase. As mentioned earlier, after the shock front propagates rapidly throughout the medium, a gas bubble begins to expand radially outward due to the high temperature and pressure of the explosive byproducts at its center. The gas bubble continues to expand radially outward as the pressure inside the bubble is greater than the pressure outside of the bubble. At some point in time, the bubble grows to the point to where the pressures inside and outside the bubble are the same, but due to its significant outward momentum, the bubble continues to expand radially outward. Eventually the momentum of the bubble expansion is overcome by the imbalance between the pressure outside of the bubble and that inside of the bubble. At this instant the bubble has reached its first bubble maximum, and there is very low pressure inside the bubble. This is manifested in the associated pressure-time history as the long duration negative pressure phase that exists for most of the duration of the bubble oscillation.

The bubble now begins its contraction phase, rapidly passing through the point of pressure equilibrium and continuing on to recompress the bubble gasses. Bubble contraction continues until the bubble cannot contract any more due to the compressibility of the gasses inside. Here the inward contraction of the bubble is rapidly reversed causing the first bubble pulse, which is evident in the corresponding pressure-time history.

In addition to the interplay of the dynamic forces associated with pressure imbalances and fluid momentum, the forces of gravity and buoyancy also affect the gas bubble dynamics. As the gas bubble expands and becomes larger in diameter, it becomes more buoyant. At the same time, as it tries to move vertically upward, fluid drag forces resist its upward migration. Eventually, after

the first bubble maximum occurs and the bubble is contracting, it begins to migrate vertically upward as the combination of bubble inward flow and buoyancy overcome the drag forces. This is depicted in the diagram in Fig. 14 as a vertical movement of the center of the gas bubble to a shallower depth. Next, the process continues with subsequent bubble expansions, contractions and pulsations, and migrations until either the gas bubble vents to the water surface or, for extremely deep detonations, all of the gas bubble energy is expended. For each of these subsequent oscillations, the maximum bubble diameters are becoming progressively smaller while the minimum bubble diameters at pulsation are becoming progressively larger. These subsequent phases are likewise accompanied with the corresponding negative pressure and bubble pulse aspects in the associated pressure-time history. Each of these pressures is diminishing in amplitude with each successive pulsation.

The primary events associated with the bubble dynamics described above and illustrated by the schematic and time-history plot of Fig. 14 will now be briefly summarized in the list below:

- Summary of General Features of Explosive Gas Bubble Dynamics:
  - Gaseous products expand outward
  - Water has large outward velocity, bubble diameter increases
  - Internal gas pressure decreases — water inertia outward
  - Outward flow eventually stops
  - Bubble contracts — water flow inward
  - Compressibility of gas stops inward motion abruptly
  - Bubble pulse occurs
  - Process of general features repeats until bubble vents to surface or energy = 0

A photograph of an underwater explosion gas bubble that has reached its maximum radius is presented in Fig. 15. From this view it can be observed that the bubble is nearly perfectly spherical in shape and has not moved much vertically since its generation.

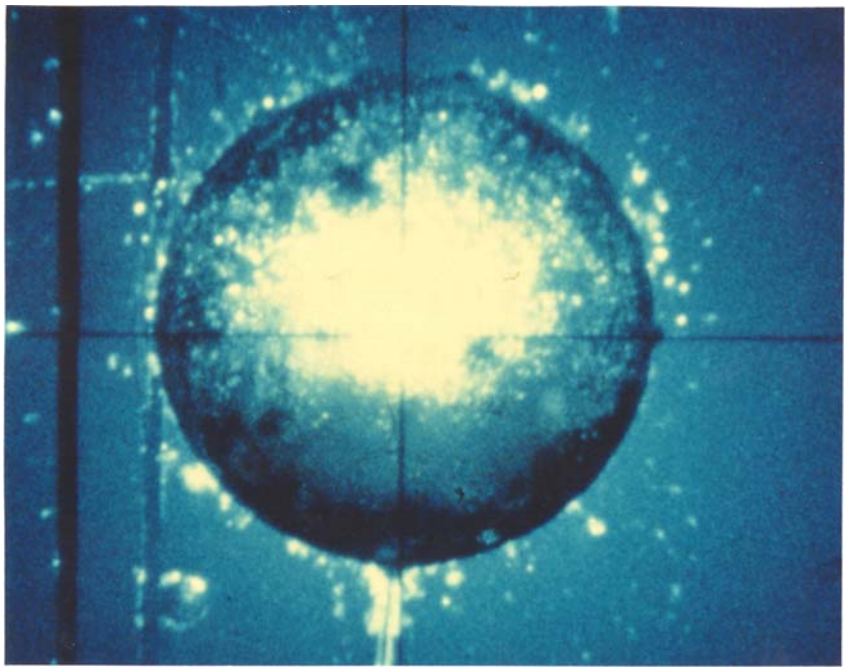

Fig. 15 – Underwater Explosion Bubble at Maximum Radius

In Fig. 16, a plot of the displacement of the gas sphere as a function of time is shown for a 300-lb TNT charge fired 50 ft below the surface. As can be observed from this plot, at the point in time where the first bubble maximum is reached, the center of the bubble has moved very little in the vertical direction. It's only during the contraction phase and first bubble pulse phase that the migration of the center of the bubble becomes significant. The small series of photographs to the right of the plot in Fig. 16 clearly illustrate the shapes and sizes of the bubble during the various phases. Moving from top left to top right, and then from bottom left to bottom right one can see the progression of bubble geometries throughout the initial expansion, contraction and pulsation phases, as well as visualize the amount of vertical migration that has taken place. Also interesting to note is the fact that during the contraction phase the bubble does not remain spherical but instead assumes a more toroidal shape as the bottom of the bubble folds inward to create a re-entrant jet during the bubble pulse. This geometric shape change coupled with the associated flow assist the bubble in its vertical migration, as mentioned previously.

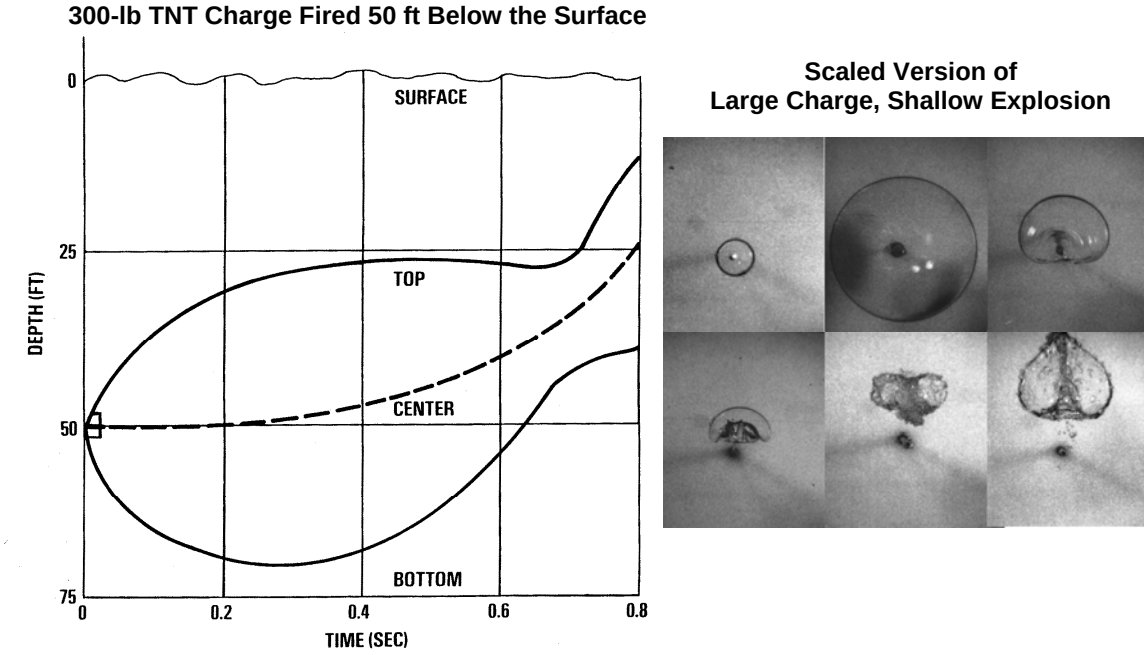

Fig. 16 – Displacement of the Gas Sphere

Measured pressure histories from a free-field UNDEX test are presented in Fig. 17. From the long-time playback of the recorded pressure-time history shown in the lower plot, one can observe the initial shock wave pressure, followed by the first and second bubble pulses. For this explosive scenario, these events all occur within one second. Above this plot are two expanded plots that more clearly illustrate the shock wave and first bubble pulse. In these plots, one can see the exponentially decaying nature of the incident shock wave, as well as the bell-shaped nature of the first bubble pulse. For this explosive scenario, the duration of the incident shock wave pressure pulse is on the order of a few milliseconds, whereas the duration of the first bubble pulse is on the order of 100 milliseconds.

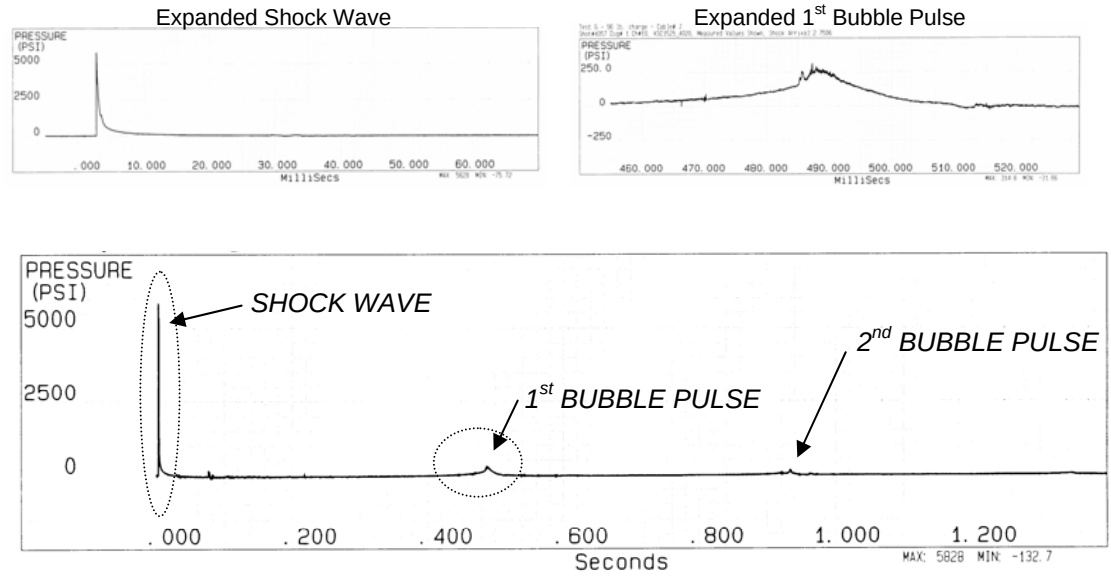

Fig. 17 – Measured Pressure History

The final aspect of bubble dynamics that will be addressed in this paper is that of bubble attraction. Fig. 18 presents a series of snapshots from a boundary element code simulation of an explosive gas bubble interacting with a rigid wall. From this series of snapshots, one can observe that the solid boundary acts as a flow obstruction and influences the motion of the gas bubble. In the first snapshot, the boundary is seen not to have much effect during the initial expansion phase. However, as the bubble begins to contract, flow on the left side of the bubble is impeded due to the presence of the rigid boundary. Thus, as the bubble contracts its left side remains virtually stationary while its right side begins moving towards the left. This significant effect results in the figure shown in the second snapshot from the left, where the bubble's shape becomes distorted and its center moves closer to the rigid plate. As the flow continues to rush around the contracting bubble, the apparent attraction to the rigid plate becomes more evident and the right side of the bubble begins to turn inward and jet towards the plate, as seen in the third and fourth snapshots, respectively. The degree of attraction depends on the charge standoff, maximum bubble radius, as well as on the size and curvature of the obstruction. Also observed from experiments is the fact that for UNDEX generated gas bubbles, the depth and orientation of the obstruction relative to gravity have a significant effect on bubble jet direction.

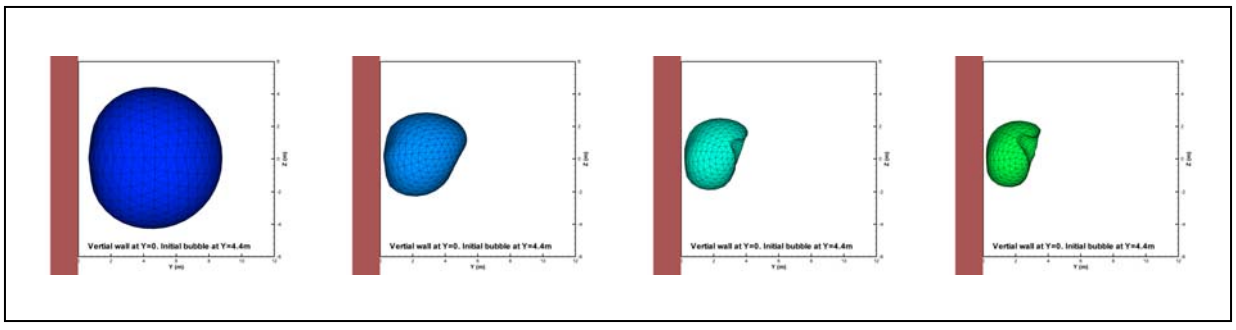

Fig. 18 – Illustration of Bubble Attraction

SURFACE EFFECTS

The next feature of UNDEX phenomena to be discussed is that of observed surface effects. To illustrate these effects, the surface phenomena observed for the detonation of a 250-lb HBX-1 explosive charge at a depth of 50-ft are sketched in Fig. 19 below. The first sketch shows the spray dome, which is caused by the interaction of the compressive shock wave with the free surface. As the shock wave is reflected back into the fluid as a tensile wave, the water particles near the surface are launched vertically upward forming a parabolic shaped spray dome. This column of water takes on a more conical shape and grows in vertical extent as the gas bubble progresses through its first expansion phase and causes a radial outward flow.

Later in time after the water column has reached its maximum size, the first gas bubble pulse occurs and results in a sharp protrusion through this column of a plume of water that is moving both vertically upward and radially outward. This radial breakout of the first plume is shown in the second sketch of Fig. 19.

As the gas bubble continues to pulsate, additional radial plumes, such as the one shown in the third sketch of Fig. 19, will be observed. In the event that the bubble migration has occurred to the point that during one of its pulsations it vents to the water surface, then the observed plume associated with that pulsation will tend to be dark in color as a result of the explosive byproducts now being released above the water surface.

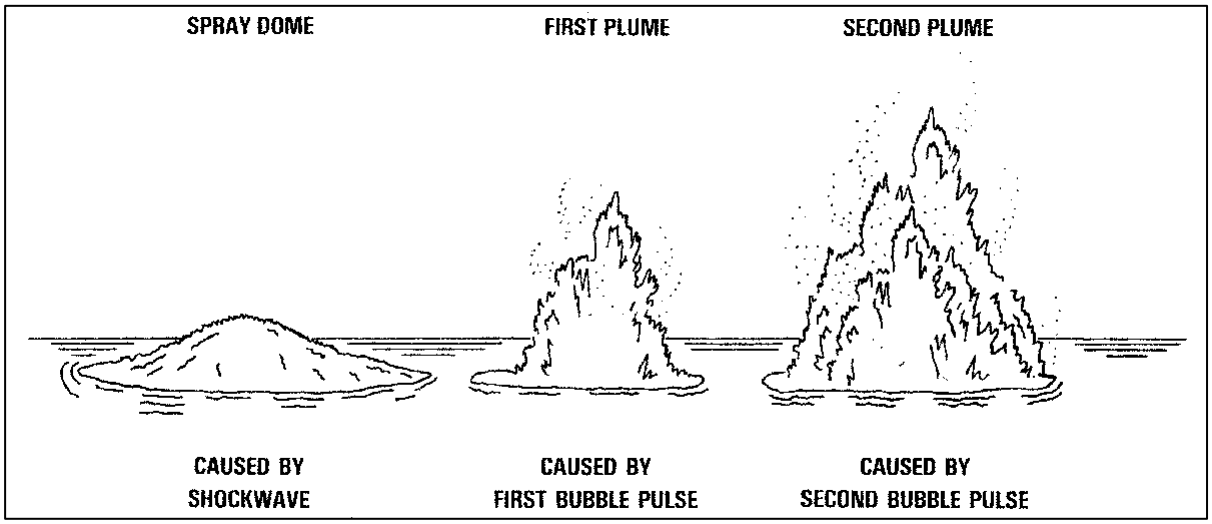

Fig. 19 – Surface Phenomena for 250-lb HBX-1 at 50-ft Depth

The surface effects associated with an underwater explosion are further illustrated with the series of photographs from an actual shock test and corresponding animations from hydrocode simulations of the same event, presented in Fig. 20. In this series of illustrations as one moves from left to right, the progression of gas bubble states is correlated with the observed surface effects. In the first pair of illustrations, the early expansion of the gas bubble is shown in the simulation, and the corresponding photograph of the surface shows the spray dome caused by the shock wave.

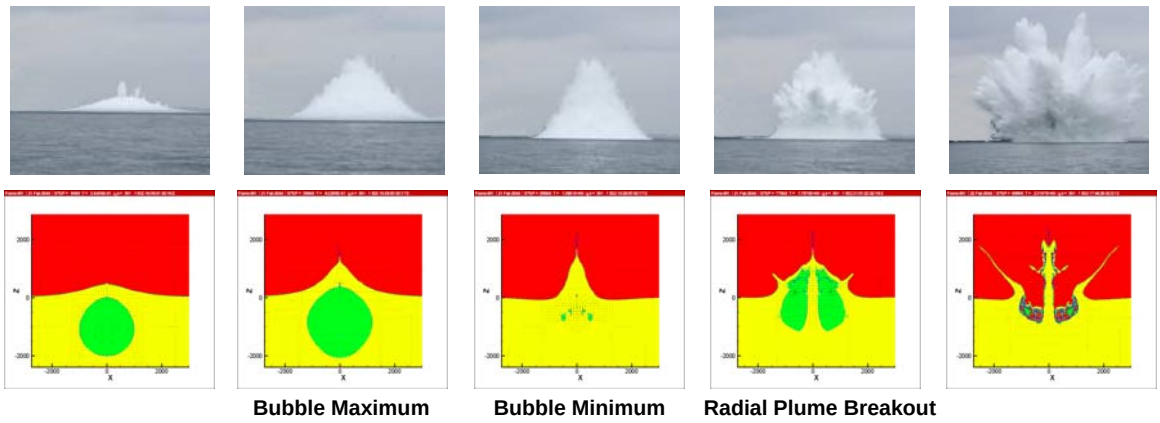

Fig. 20 – UNDEX Plume Above-Surface Effects

The second pair of illustrations shows the bubble at its maximum, corresponding to photo above it of the surface state showing a conical-shaped water column. The water column has progressed in vertical extent as can be observed in the third set of illustrations, where the gas bubble is now shown to be at its first minimum.

The last two sets of illustrations show the corresponding simulation results and above water photographs of the early and late phases, respectively, of the radial breakthrough of the first plume. These surface states occur following the first bubble pulse, as was described earlier.

The extent and characteristics of the observed surface effects will vary with the explosive charge size, depth of charge detonation, and proximity of reflecting boundaries such as the ocean bottom. The illustration presented above, however, should enable the reader to make a general connection between the observed events above the water surface and the shock wave and bubble dynamics that are occurring below the surface.

SHOCK WAVE REFRACTION EFFECTS

The final element of UNDEX phenomena to be addressed is that of shock wave refraction. For an UNDEX event, the influence of refraction on the shock wave propagation becomes of great interest for scenarios that involve large standoff ranges where the fluid medium can have varying thermal conditions. In this situation, the assumptions of linear acoustic propagation of the incident shock wave begin to break down in that the thermal gradients bring about changes in the propagation speed and thus have the effect of causing the shock wave to bend along its path from the charge source to the target. As a result, the propagation of the incident shock wave will be modified in terms of both speed and direction.

These shock wave refraction effects can be best described by studying the series of plots and diagrams presented in Fig. 21. In this figure, a series of ray tracing plots generated by the REFMS code [4] for five UNDEX tests involving long standoff ranges at decreasing standoff are depicted. Alongside these plots are the corresponding measured sound velocity profiles from the ocean environment at the test site. These sound velocity profiles are represented by the vertical plots to the left of each ray tracing plot and show the variation of sound velocity in the medium as a function of depth. From these curves, it is evident that the sound velocity values fluctuate significantly for each test. Each ray tracing plot, on the other hand, shows the various paths that

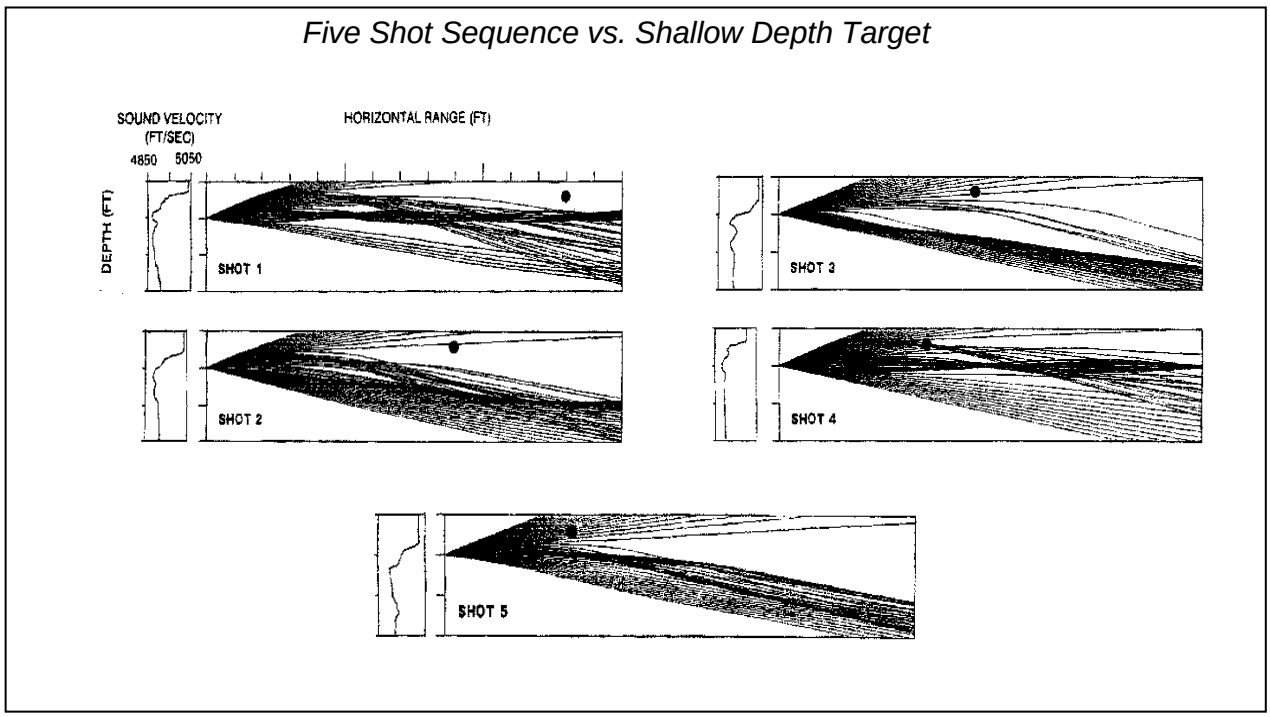

Fig. 21 – Observed Shock Wave Refraction Effects

the shock wave takes as it propagates from the charge source on the left side of the plot to the target represented by the black dot to the right.

The plot set on the top left of Fig. 21 represents the condition for Shot 1, where the explosive charge was the furthest from the target. In this case, from the ray tracing curves it can be observed that all of the paths that the shock wave takes from the charge location bend in such a wave that by the time they reach the range where the target is located, they completely fall below the target. Thus, for this particular test, significantly lower shock wave effects were experienced at the target than had been estimated assuming iso-velocity water.

As one progresses through the test series and examines the ray tracing plots associated with Shots 2 and 3, where the target is located increasingly closer to the charge, the effects of shock wave refraction are still evident, but these are diminishing as the standoff distance decreases. For Shot 4, however, one can notice the fact that the bending shock wave paths actually converge at the position of the target, focusing the shock wave effects at this location. In the ray tracing plot for Shot 5, however, the focusing effect is less pronounced as it was for Shot 4. The characteristics of the sound velocity profiles for these two tests were also different. The overall effect of these variations was that even though the charge standoff for Shot 4 was larger than that of Shot 5, the shock wave focusing effect brought about by refraction caused the levels of shock wave energy experienced by the target to be nearly the same for these two tests.

Thus, from the example presented above in Fig. 21, refraction effects can significantly alter the propagation of the shock wave and the energy that eventually is imparted to the target. This is especially significant for test scenarios involving large standoff ranges and varying sound velocity profiles. These effects must be accounted for, especially if one desires to apply scaling techniques to the resulting dynamic loading or target response data.

SUMMARY

This report introduced and briefly described the basic elements of underwater explosions and shock physics. From the details and examples that are presented, it is clear that UNDEX phenomena are indeed both fascinating and complex. The illustration presented in Fig. 22 below summarizes each of these basic features in a single diagram. From this figure one can clearly see the various paths of the direct shock waves, the surface reflected wave, the bottom reflected waves traveling directly through the fluid and traveling partially through the bottom material, the bulk cavitation region, the gas bubble migration and pulsation, and the various associated surface phenomena. All of these phenomena, along with the effects of shock wave refraction, are important to accurately defining the dynamic loading environment that occurs throughout the fluid medium and can affect any structure that is present.

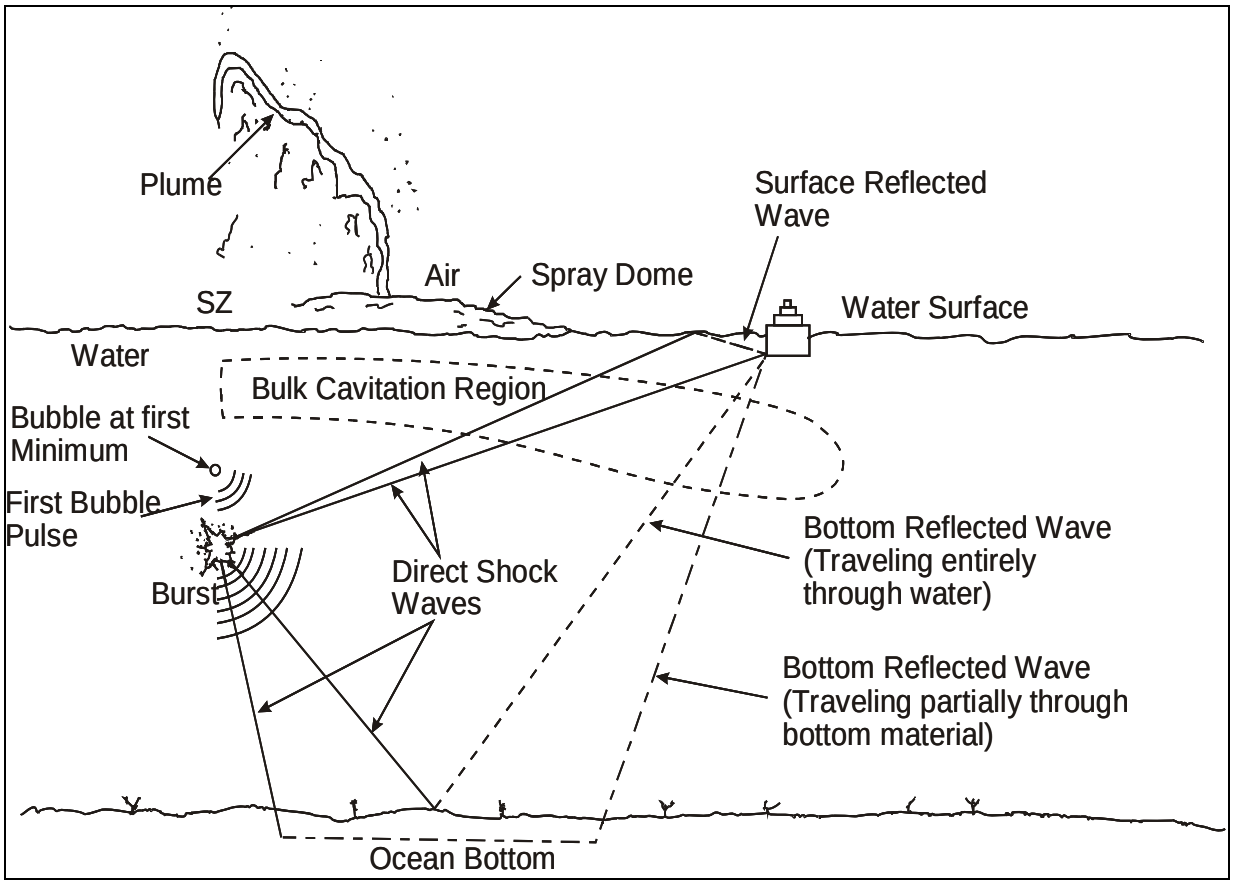

Fig. 22 – Summary of Underwater Explosion Phenomena

Finally, the information presented within this report provides a basic introduction to the basic phenomena associated with underwater explosions. The objective was to provide a detailed enough introduction of these phenomena that the reader would obtain both a deeper understanding of the basic physics involved and a stimulated interest in the subject.

REFERENCES

1. Cole, Robert H., “Underwater Explosions,” Princeton University Press, 1st Edition, 1948.

2. Costanzo, Frederick A., and John D. Gordon, “A Solution to the Axisymmetric Bulk Cavitation Problem,” 53rd Shock and Vibration Bulletin, Shock and Vibration Information Center, Naval Research Laboratory, Washington, D.C., May 1983.

3. Snay, H. G., “Hydrodynamics of Underwater Explosions,” Naval Hydrodynamics Publication 515, National Academy of Sciences – National Research Council, 1957.

4. Britt, J. R., R. J. Eubanks and M. G. Lumsden, “Underwater Shock Wave Reflection and in Deep and Shallow Water: Volume I – A User’s Manual for the REFMS Code (Version 4.0),” Science Applications International Corporation, St. Joseph, LA., DNR-TR-91-15-VI, 1991.